Mesoporous Silica Nanoparticles Coated by Layer-by-Layer Self-assembly Using Cucurbit[7]uril for in Vitro and in Vivo Anticancer Drug Release

Qing-Lan Li,[†] Yanfang Sun,[†,‡] Yu-Long Sun,[†] Jijie Wen,[‡] Yue Zhou,[†] Qi-Ming Bing,[†] Lyle D. Isaacs,[§] Yinghua Jin,[∥] Hui Gao,*[‡] and Ying-Wei Yang*[†]

[†]State Key Laboratory of Supramolecular Structure and Materials, College of Chemistry, International Joint Research Laboratory of Nano-Micro Architecture Chemistry (NMAC) and [∥]Key Laboratory for Molecular Enzymology & Engineering, Ministry of Education, Jilin University, 2699 Qianjin Street, Changchun, 130012 P.R. China

[‡]School of Chemistry and Chemical Engineering, Tianjin University of Technology, Tianjin, 300384 P.R. China

[§]Department of Chemistry and Biochemistry, University of Maryland, College Park, Maryland 20742-4454, United States

Ⓢ *Supporting Information*

ABSTRACT: Mesoporous silica nanoparticles (MSNs) are promising solid supports for controlled anticancer drug delivery. Herein, we report biocompatible layer-by-layer (LbL) coated MSNs (LbL-MSNs) that are designed and crafted to release encapsulated anticancer drugs, e.g., doxorubicin hydrochloride (DOX), by changing the pH or by adding competitive agents. The LbL coating process comprises bis-aminated poly(glycerol methacrylate)s (BA-PGOHMAs) and cucurbit[7]uril (CB[7]), where CB[7] serves as a molecular bridge holding two different bis-aminated polymeric layers together by means of host–guest interactions. This integrated nanosystem is tuned to respond under specific acidic conditions or by adding adamantaneamine hydrochloride (AH), attributed to the competitive binding of hydronium ions or AH to CB[7] with BA-PGOHMAs. These LbL-MSN hybrids possess excellent biostability, negligible premature drug leakage at pH 7.4, and exceptional stimuli-responsive drug release performance. The pore sizes of the MSNs and bis-aminated compounds (different carbon numbers) of BA-PGOHMAs have been optimized to provide effective integrated nanosystems for the loading and release of DOX. Significantly, the operating pH for the controlled release of DOX matches the acidifying endosomal compartments of HeLa cancer cells, suggesting that these hybrid nanosystems are good candidates for autonomous anticancer drug nanocarriers actuated by intracellular pH changes without any invasive external stimuli. The successful cellular uptake and release of cargo, e.g., propidium iodide (PI), in human breast cancer cell line MDA-231 from PI-loaded LbL-MSNs have been confirmed by confocal laser scanning microscopy (CLSM), while the cytotoxicities of DOX-loaded LbL-MSNs have been quantified by the Cell Counting Kit-8 (CCK-8) viability assay against HeLa cell lines and fibroblast L929 cell lines. The uptake of DOX-loaded LbL-MSNs by macrophages can be efficiently reduced by adding biocompatible hydrophilic poly(ethylene glycol) or CB[7] without destroying the capping. In vivo tumor-growth inhibition experiments with BALB/c nude mice demonstrated a highly efficient tumor-growth inhibition rate of DOX-loaded LbL-MSNs, suggesting that the novel type of LbL-MSN materials hold great potentials in anticancer drug delivery.
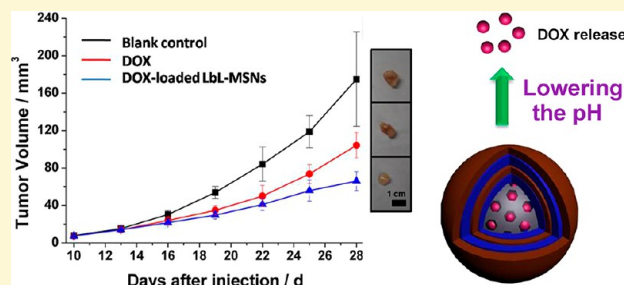
Recently, controlled release nanosystems based on a wide range of materials, capable of selectively releasing cargo, that is, anticancer drugs and labeling dyes, under different external stimuli, have demonstrated their viability for use in a variety of biological applications, for example, bioimaging, tumor therapy, and anticorrosion coatings.[1−10] Among these, inorganic mesoporous materials and stimuli responsive polymers have been employed widely in the construction of controlled release systems.[8,11] Early in 2001, Vallet-Regí et al.[12] proposed that MCM-41-type mesoporous silica nanoparticles (MSNs) are ideal candidates for drug delivery. Thereafter, MSNs have been used widely as platforms and nanocarriers for cargo storage, controlled release, and gene transfection. The rapid adoption of MSNs can be attributed to their superior properties, that is, good biocompatibility, structural rigidity, chemical stability, optical transparency, high surface areas, large pore volumes, uniform and tunable pore sizes, and controllable surface functionalization.[8,12−15] The application of conventional MSNs as delivery vehicles, however, is limited by the spontaneous leakage of cargo molecules from MSNs during the material preparation step and the premature release in the course of cargo delivery. Especially for theranostic nano-
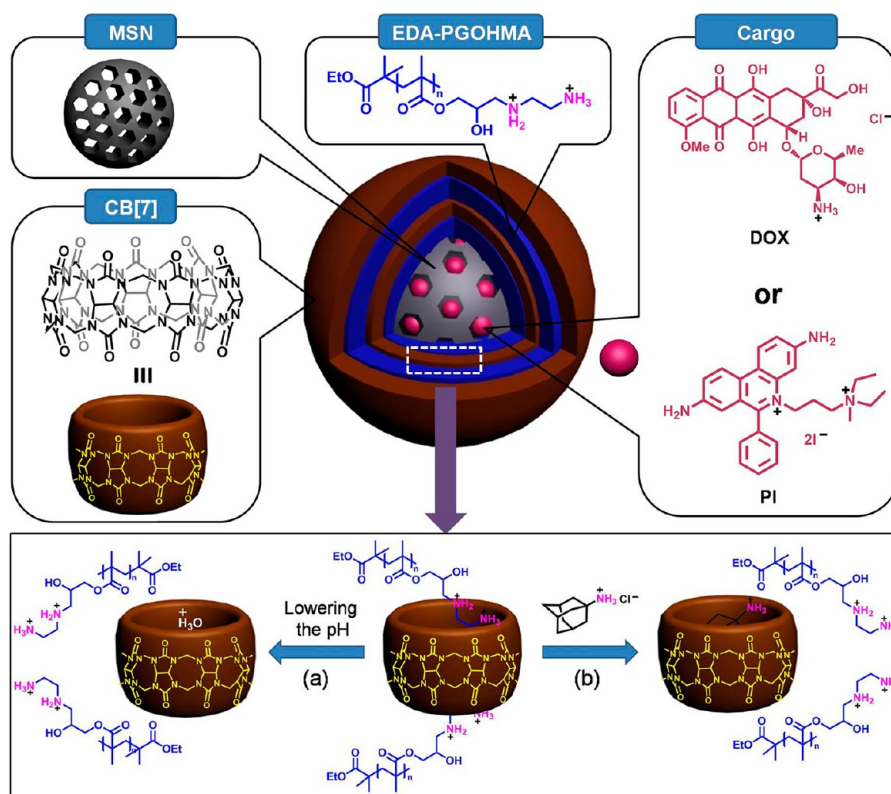
Figure 1. Schematic diagram of LbL-MSN nanocontainer based on EDA-PGOHMA. The LbL systems on the surface of MSNs were operated by lowering the pH value or adding adamantaneamine hydrochloride (AH) to regulate the release of cargo, i.e., anticancer drugs (doxorubicin hydrochloride (DOX)) or dye molecules (propidium iodide (PI)). (a) Lowering the pH value to form strong ion−dipole interactions between CB[7]s and plentiful hydronium ions, and then compel CB[7] layer to dissociate with polymer layers; (b) addition of AH to induce the release of CB[7], and cargo, from the LbL film.

medicine, delivery and on-demand release of drugs using these first-generation MSNs cannot be accomplished with precise control over the target location. Early examples of gated delivery systems based on MSNs were reported by Fujiwara and co-workers[16] and Lin and co-workers[17] where coumarin photodimerization and CdS quantum dots are used to regulate the gates. Stoddart, Zink, and co-workers[18] reported a novel supramolecular nanovalve system, where a layer of pseudor-otaxanes consisting of 1,5-dioxynaphthalene units encircled by cyclobis(paraquat-*p*-phenylene) rings is installed onto the pore orifices of MSNs to control the release of cargo molecules loaded inside MSNs under redox control. For further optimization and practical applications of these gated smart delivery vehicles, a variety of pore blockers/regulators have been developed during the past decade, using organic molecules,[16,19] inorganic nanoparticles,[20,21] (bio)polymers,[22] and supramolecular molecular machines.[14,18,23−35] Meanwhile, various physical and chemical stimuli, such as redox,[18,23] light,[16,24−26,36−41] pH,[23,24,27,28,30,42,43] temperature,[31] compet-itive binding,[32] and enzymes[33,35,44] have been used to switch on/off the gatekeepers, thereby regulating the release of entrapped cargo molecules.

Among the stimuli explored previously, targeted controlled release based on pH changes has gained considerable attention. It represents an efficient strategy for cancer therapy because of the pH difference between tumor cells and normal cells/bloodstream which can be used to target tumor cells selectively.[45,46] Compared with the neutral pH values (7.4) of blood and normal tissues, the tumor extracellular environment

is slightly acidic (pH 6.8). Notably, the pH values of endosome and lysosome in tumor cells are lower at 5.0−5.5, presenting apparent acidity. Indeed, pH-responsive drug delivery systems based on mesoporous materials remain one of the most actively investigated drug delivery systems. In the past, pH-responsive systems have relied upon supramolecular nanovalves, pH-cleavable linkers, acid-degradable caps, polyelectrolytes, and coordination polymer nanoparticles as release triggers.[19,21,22,46]

Polymers have also proved to be excellent material for the construction of drug delivery systems. Over the past few years, poly(glycerol methacrylate)s (PGOHMAs) have emerged as an efficient alternative to classical polymers. PGOHMAs are employed in many research fields on account of their straightforward synthesis from readily available low-cost starting materials, good natural biocompatibility, easy chemical modifications/grafting/cross-linking, and excellent physico-chemical properties.[47−51] Previously, we have shown that nanocapsules fabricated from star-shaped bis-aminated PGOH-MA (BA-PGOHMA) and poly(acrylic acid) (PAA) using the layer-by-layer (LbL) self-assembly method are pH-responsive and undergo targeted release of their cargo, indicating they are promising candidates as gate components on MSNs for drug delivery and gene therapy.[52−55] In the conventional polymeric nanocarrier systems, the cargo are usually linked covalently or attached noncovalently to the supporting materials by weak van der Waals interactions, and are released upon application of appropriate stimuli.[11] On the other hand, supramolecular polymers have been utilized for controlled cargo release because of their unique abilities as superamphiphilic polymers[56]
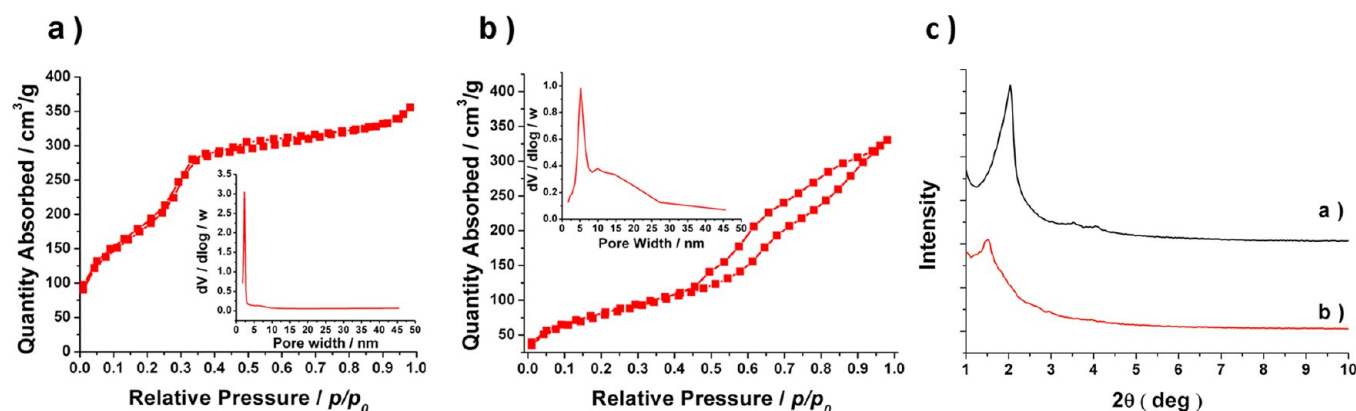
Figure 2. (a) BET isotherm and BJH pore size distribution (inset) of MSN-1; (b) BET isotherm and BJH pore size distribution (inset) of MSN-2; (c) small-angle XRD patterns of MSN-1 (black) and MSN-2 (red).

Table 1. Properties of the MSNs Calculated from the Small-Angle XRD Patterns and N_2 Adsorption−Desorption Isotherms

samples	interplanar spacing, d_{100} [nm]	pore distance [nm]	S_{BET} [m²/g]	V_p [mL/g]	D_1 [nm]	D_2 [nm]	D_3 [nm]
MSN-1	3.91	4.52	692	0.45	2.80	2.47	2.60
MSN-2	5.25	6.07	291	0.48	5.20	4.73	6.60

and LbL materials.[52,57−66] To the best of our knowledge, however, stimuli-responsive LbL supramolecular polymers have not been employed as gating materials on MSN surfaces for controlled drug delivery. In this paper, we demonstrate that cucurbit[7]uril[67−76] (CB[7]) can serve as a kind of supramolecular glue[77] between layers of BA-PGOHMA polymers, i.e., EDA-PGOHMA, BDA-PGOHMA, and HDA-PGOHMA derived from 5-arm poly(glycidyl methacrylate) (PGMA) with ethanediamine (EDA), 1,4-butanediamine (BDA), and 1,6-hexamethylenediamine (HDA), respectively, via ion−dipole interactions to form stable supramolecular polymers on the surface of cargo-loaded MSNs (Figure 1). We further envision that such supramolecular polymers will respond to suitable stimuli (e.g., pH or competitive guest) to release the encapsulated cargo, e.g., doxorubicin hydrochloride (DOX) and propidium iodide (PI).

RESULTS AND DISCUSSION

Design and Synthesis of LbL-MSNs. Self-assembly on the surface of mesoporous materials has proven to be a practical approach for the development of nanoscale hybrid materials for controlled drug release. Many of the previous examples take advantage of (macro)molecular or supramolecular interactions to build nanovalves or nanogates for the tuning of the pore sizes and pore openings. Herein, by employing LbL self-assembly technology, we have constructed supramolecular polymer coatings on the surface of MSN-based drug nanocarriers as pH-sensitive drug delivery systems. To compare the influence of pore size on loading capacity, two types of MSNs with different pore sizes were prepared using a template-directed sol−gel method with a single or compound surfactant. Traditionally, cetyltrimethylammonium bromide (CTAB) has been used as a template and tetraethoxysilane (TEOS) as the source of the silica, followed by the removal of template through extracting the nanoparticles with acidified MeOH to give traditional MSNs, that is, MSN-1 with a pore diameter of ca. 2.7 nm. Swollen MCM-41 nanoparticles, that is, MSN-2 with a pore diameter of ca. 5 nm, was obtained by using 1,3,5-trimethylbenzene as an assistant template, mixed with CTAB as a compound surfactant. The empty nanopores were loaded

with DOX by soaking MSNs in a 0.5 mM solution of DOX for 5 h, prior to being used for controlled release performance studies.

After loading DOX within MSNs, the LbL coating in addition to CB[7] on the negatively charged surface of MSNs, alternately, above the isoelectric point was initiated. Therefore, the first layer was coated with the positively charged polycationic EDA-PGOHMAs by means of electrostatic interactions, and then CB[7]s were assembled with BA-PGOHMAs by dint of host−guest interactions. Supramolecular multilayer coatings on MSNs can be prepared sequentially. The MSNs can be used as reservoirs for cargo and the supramolecular self-assembly coatings as the stimuli-responsive nanocaps. Notably, the theoretical storage capacity of this system has been increased, the stimuli-responsive release of drug molecules has been achieved, and the mechanical resistance of the nanocarriers to the environment has been enhanced by coating them with supramolecular multilayers composed of polyelectrolytes and synthetic macrocycles.

Material Characterization. According to N_2 adsorption and desorption isotherms (Figure 2a,b), an adsorption step at P/P_0 value (0.1−0.3) of two types of MSNs exhibits characteristic type IV isotherms, confirming the presence of typical mesoscale pores. The step is obtained because of the nitrogen condensation inside the mesopores by capillarity. The Brunauer−Emmett−Teller (BET) model works out the specific surface (S_{BET}) value of the two types of MSNs as shown in Table 1. In addition, a pronounced step is displayed at relative pressures ranging from 0.2 to 0.7 (P/P_0) because of the capillary condensation of nitrogen inside the primary mesoporous material. A narrow Barrett−Joyner−Halenda (BJH) pore size distribution was indicated in accordance with the steep condensation step and the pore volumes of two types of MSNs are displayed in Table 1. There are three different methods to calculate the pore sizes of the materials: (a) the BJH method; (b) geometrical considerations of an infinite hexagonal array of cylindrical pores, expressed by averaged pore diameter (APD) (eqs 1),

$$APD = 1.213 d_{100}(\rho V_p/(1 + \rho V_p))^{1/2} \tag{1}$$

and (c) the model of simple cylindrical pores using the BET surface area (eqs 2),

$$D_p = 4V_p/S_{BET} \qquad (2)$$

Figure 2c shows the small-angle XRD patterns of MSN-1 and MSN-2. The pore distance between adjacent pores of these MSNs can be evaluated by Bragg equation.

According to the Bragg equation (eqs 3),

$$2d \sin \theta = n\lambda (n = 1; \lambda = 1.392218) \qquad (3)$$

Interplanar spacing d (eqs 4),

$$d = n\lambda/2 \sin \theta \qquad (4)$$

100 interplanar spacing d_{100} (eqs 5),

$$d_{100} = \lambda/2 \sin \theta \qquad (5)$$

Pore distance a (eqs 6),

$$a = (2/1.732)d_{100} = 1.155\lambda/(2 \sin \theta) \qquad (6)$$

The position of the main (100) peak was used to calculate the interplanar spacing d_{100} and the pore distances for MSN-1 and MSN-2 (Table 1).

TEM and SEM (Figures 3 and S3) indicate that the two types of MSNs are spherical in shape, with an average particle
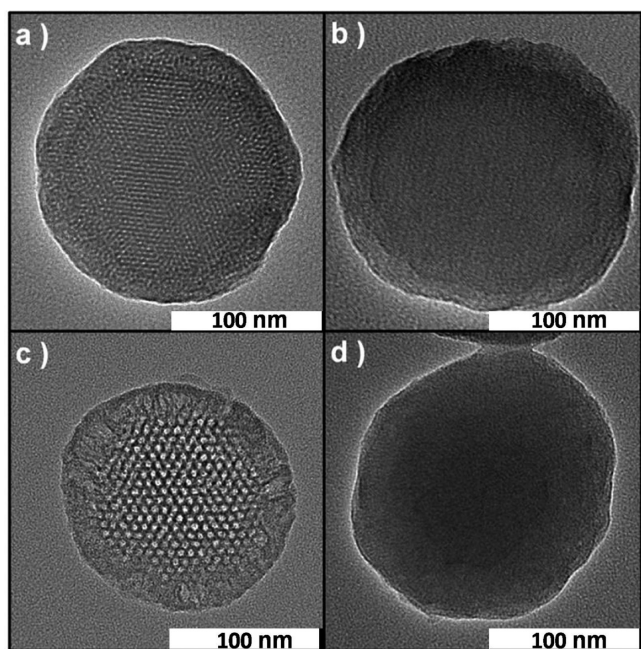

Figure 3. TEM images: (a) MSN-1; (b) DOX-loaded, LbL self-assembly MSN-1 based on EDA-PGOHMA and CB[7] (LbL-MSN-1); (c) MSN-2; (d) DOX-loaded, LbL self-assembly MSN-2 based on EDA-PGOHMA and CB[7] (LbL-MSN-2).

size of ca. 190 nm in diameter. Before DOX loading and LbL self-assembly on the surface of nanoparticles, MSN-1 exhibits uniformly sized 2D-hexagonally ordered cylindrical pores, whereas MSN-2, although it has the same pore arrangement as MSN-1, has bigger pore sizes (ca. 5.5 nm for MSN-2 and ca. 2.7 nm for MSN-1). Both MSN-1 and MSN-2, after DOX-loaded and LbL self-assembly, however, barely exhibit pore structures on account of the surface coating of supramolecular polymeric layers. The average sphere diameter after self-assembly becomes ca. 200 nm owing to the self-assembly layers

of ca. 5–10 nm in thickness on the surfaces of MSN-1 and MSN-2 (Figure S3).

Thermogravimetric analysis (TGA) curves of MSN-1, MSN-2, DOX-loaded MSN-1, DOX-loaded MSN-2, DOX-loaded LbL-MSN-1, and DOX-loaded LbL-MSN-2 are shown in Figure 4 and Table 2. All of the weight losses were detected from 180 to 900 °C and all the samples showed weight losses below 180 °C that resulted from the physical loss of water. Because organic silica was modified on the surface of MSN-1 in the course of synthesis, the weight loss of MSN-1 is more than that observed for MSN-2 (Table S1). Although MSN-2 can load more DOX molecules, a mass of DOX molecules will be lost during the process of self-assembly because of the lower specific surface area (Figure 4a,b). In the LbL-MSN materials, the loss of 9.1% (or 12.2%) of weights between 180 and 370 °C can be attributed to the removal of DOX and EDA-PGOHMA from the systems, while the other weight losses (18.0% or 17.9%) can be attributed to the removal of CB[7] compounds when the temperature is higher than 370 °C (Table 2).

In addition, FT-IR spectroscopy was used to monitor the LbL self-assembly of MSN-1 and MSN-2: this technique provides evidence for and proved clearly the successful modification because the characteristic absorption peaks of each material were observed in the final products (Figure 4c,d). There is no new chemical bond formation during loading and self-assembly; the corresponding absorptions of all the materials are observed in the FT-IR spectra of DOX-loaded LbL-MSN-1 and DOX-loaded LbL-MSN-2.

Drug Release Studies. The two drug delivery systems were investigated upon activation by changing the pH (Figure 5). At physiological pH (pH = 7.4), the positively charged EDA-PGOHMA encircles the negatively charged MSN surfaces as a result of electrostatic interactions. Meanwhile, in the multiple layer coating process, EDA-PGOHMA forms host–guest complexes by cation–dipole interactions with the uridyl carbonyl portals of CB[7] macrocycles. Upon acidifying the solution, CB[7]s would more likely form strong ion–dipole interactions with plentiful hydronium ions instead of the original diamino entities of the EDA-PGOHMAs in the supramolecular polymer coatings, and resulted in the disassociation of supramolecular multilayers, leading to the uncovering of the nanopores and thus the release of the cargo.

To demonstrate the functioning of the as-synthesized nanocarriers, the two LbL-MSNs were loaded with DOX. The release of the encapsulated drug molecule was first tested in aqueous solution with the pH stimulus. The dialysis bags containing samples of MSNs were dipped into different PBS buffers of increasing acidity (pH = 7.4, 5.0, and 2.0, respectively) and were rocked in a homothermal shaker (37 °C). DOX release from the nanopores of the MSNs was monitored by UV–vis absorption spectroscopy (Figure 5). A relatively flat baseline indicates that DOX molecules are held tightly within the nanopores of these materials at physiological pH (pH = 7.4). When the pH of the solution was lowered to 5, the interaction between CB[7] and EDA-PGOHMA layers loosens and DOX cargo was released. And at the lower pH value (e.g., pH = 2), the association of CB[7] and the diamino entities of the EDA-PGOHMAs is decreasing as hydronium ions compete with diamino entities to bind CB[7]. Most of the CB[7] molecules were taken away from EDA-PGOHMA layers by excessive hydronium ions in solution, leading to a fast release of cargo as a consequence of the breaking of the supramolecular polymeric coating. Notably, MSN-2 showed a
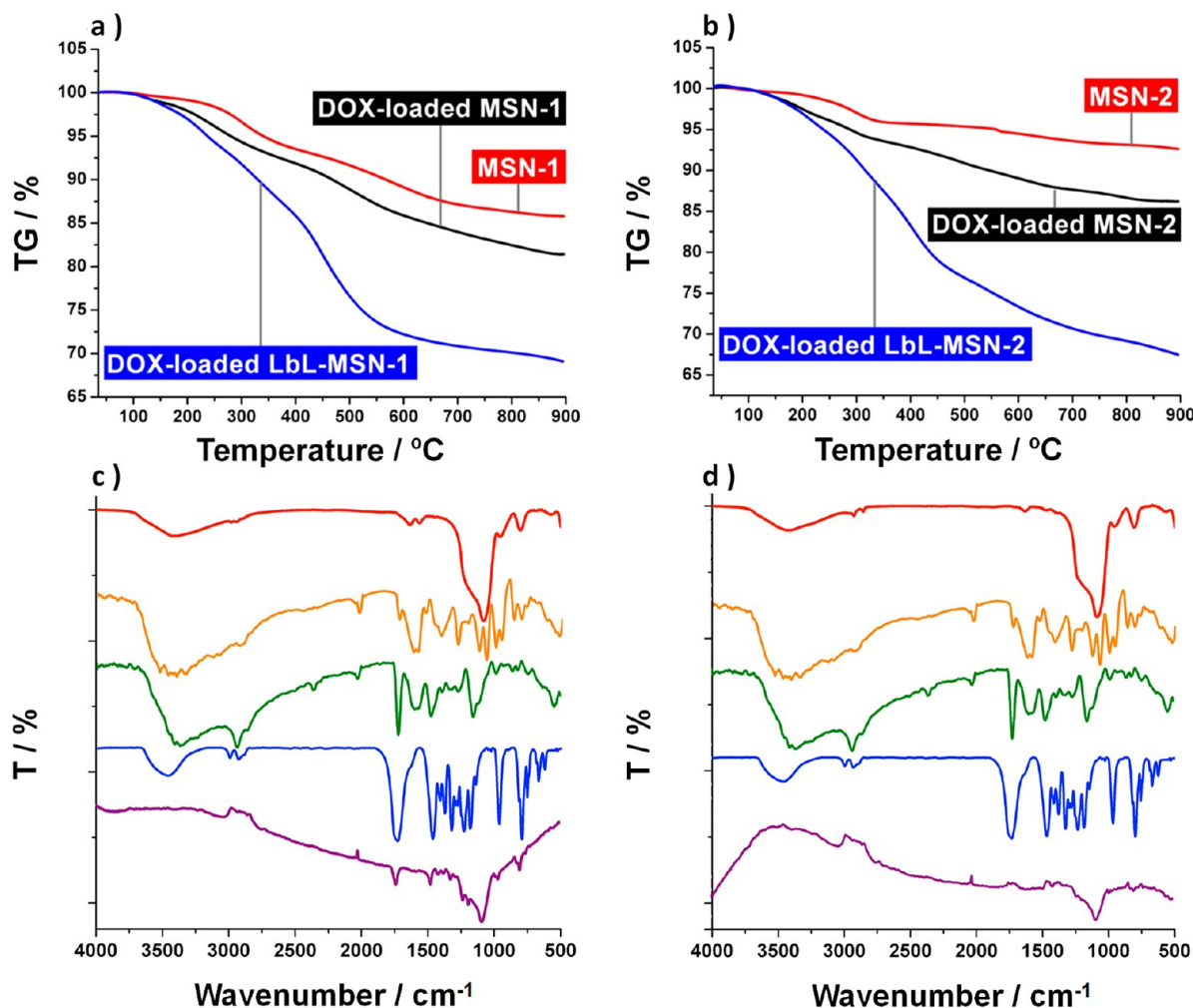
Figure 4. TGA curves: (a) i, MSN-1; ii, DOX-loaded MSN-1; iii, DOX-loaded LbL-MSN-1. (b) i, MSN-2; ii, DOX-loaded MSN-2; iii, DOX-loaded LbL-MSN-2. FT-IR spectra (KBr): (c) MSN-1 (red), DOX (orange), EDA-PGMA (green), CB[7] (blue), and DOX-loaded LbL-MSN-1 (purple); (d) MSN-2 (red), DOX (orange), EDA-PGMA (green), CB[7] (blue), and DOX-loaded LbL-MSN-2 (purple).

Table 2. TGA Results for DOX-Loaded LbL-MSN-1 and DOX-Loaded LbL-MSN-2

samples	35−180 °C [wt %]	180−370 °C [wt %]	370−900 °C [wt %]
DOX-loaded LbL-MSN-1	2.6	9.1	18.0
DOX-loaded LbL-MSN-2	2.4	12.2	17.9

lower specific cargo-loading capacity (Figure S5) because of the relatively lower specific internal area even though it has larger pore size.

In addition to the pH stimulus, the release effect of cargo was also investigated under competitive binding control. Upon the addition of AH, which possesses a much higher binding affinity ($K_a = 4.2 \times 10^{12}$ M^{-1}) toward CB[7],[78] into a cuvette containing LbL-MSNs, a soft release of the cargo molecules is observed as a result of the AH-induced dethreading of the CB[7] rings from the LbL self-assembly coatings of the MSNs. The experimental data of DOX release are summarized in Table 3.

Since the EDA-PGOHMA forms stable complex with CB[7] at suitable pH values, we believe that the alkyl chain length of bis-amino entities in the PGOHMAs might affect the cargo

loading and release behavior. This idea is based on the difference of binding stabilities of CB[7] and different bis-amines of PGOHMAs. Hence, we designed and investigated three types of BA-PGOHMAs, namely EDA-PGOHMA, BDA-PGOHMA and HDA-PGOHMA, with increasing alkyl spacers between the two amino groups (Scheme 1). Interestingly, EDA-PGOHMA possesses (Table 4) the best release performance. This apparent superiority of the short EDA-PGOHMA derivatives could be associated with the fact that they can allow the formation of more stable 1:2 host−guest complexes with CB[7], as supported by computational modeling (Figure 6).

To investigate the binding modes of EDA with CB[7], a quantum chemical calculation was performed. Because of computational limitations imposed by the large size and complexity of the present macrocyclic systems, the calculations were carried out for the most part using the semiempirical molecular orbital method, where the PM6 method was used, as implemented in Gaussian03. Although this method gives poor accuracy in the energy and the frequency compared with the ab initio method, the results of PM6 method can be considered only as a qualitative estimate of how EDA binds to CB[7].

First, we applied geometry optimization on the system of CB[7] with two EDA molecules located vertically outside the CB[7] pointing toward its geometric center, simulating the
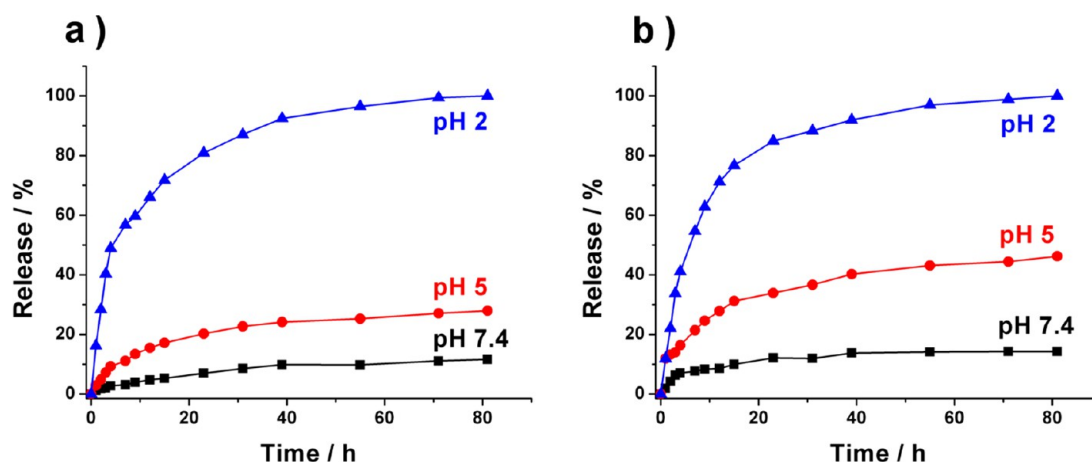
6422

dx.doi.org/10.1021/cm503304p | Chem. Mater. 2014, 26, 6418−6431

Figure 5. Release profiles of DOX from (a) DOX-loaded LbL-MSN-1 and (b) DOX-loaded LbL-MSN-2 operated at different pH conditions. The released DOX concentration was monitored by UV–vis absorption spectroscopy (the detection wavelength is 498 nm). For both systems, no appreciable cargo leakage was observed at physiological pH, but under more acidic conditions, the chemotherapeutic guest molecules were released.

Table 3. Comparison of Release Efficiency between pH Changes and AH Addition (Setting Changing pH to 2 as 100%)

control methods	relative DOX release [%]	
	DOX-loaded LbL-MSN-1	DOX-loaded LbL-MSN-2
changing pH to 2	100	100
adding AH	25.3	28.1

Table 4. Relative DOX Release (pH = 2) of DOX-Loaded LbL-MSN-1 and DOX-Loaded LbL-MSN-2 Based on Three Types of PGOHMAs

LbL materials	DOX-loaded LbL-MSN-1 [%]	DOX-loaded LbL-MSN-2 [%]
EDA-PGOHMA and CB[7]	100	100
BDA-PGOHMA and CB[7]	78.6	69.9
HDA-PGOHMA and CB[7]	73.4	68.9

state of the EDA molecule approaching CB[7] in the solution. After optimization, the two EDA molecules lie parallel in both entrances of one CB[7], as shown in Figure 6a,b.

Then, Multiwfn, open source software for wave function analysis, was utilized to generate the electron density maps to identify the binding sites. From the electron density map shown in Figure 6c,d, it is apparent that the local electron density of the nitrogen atoms and the closest highlighted oxygen atoms are of relatively high level; meanwhile, other oxygen atoms possess a relatively low level of electron density, which implies an existing localized electrostatic interaction between the nitrogen and the highlighted oxygen atoms. By making comparison with the local electron density of the O ring (Figure 6c,d), we confirmed the binding sites and geometry.

In Vitro Controlled Release and Cell Viability Assays. To assess whether the LbL-MSNs can be used as effective drug

nanocarriers for cancer therapy,[79] in vitro studies (Figure 7) were carried out on the human breast carcinoma cell line (MDA-MB-231). Good cell uptake of nanocarriers can enhance the delivery efficiency and achieve better therapeutic effect. To detect the uptake and cargo release behavior of the LbL-MSNs inside the cells, a membrane-impermeable dye, PI,[80] was used as a fluorescent probe and loaded into the particles following the same protocol used for DOX loading. The cells were seeded in an untreated tissue culture dish with a cover glass bottom and allowed to attach overnight. The culture media was replaced with the culture medium containing the PI-loaded LbL-MSNs and incubated for 2–24 h at 37 °C. Noticeably, the LbL-MSNs were poorly dispersed in a culture medium, a situation which was effectively solved by simply vortexing and

Scheme 1. Assembly Route Toward MSNs Capped with EDA-PGOHMA and CB[7][a]
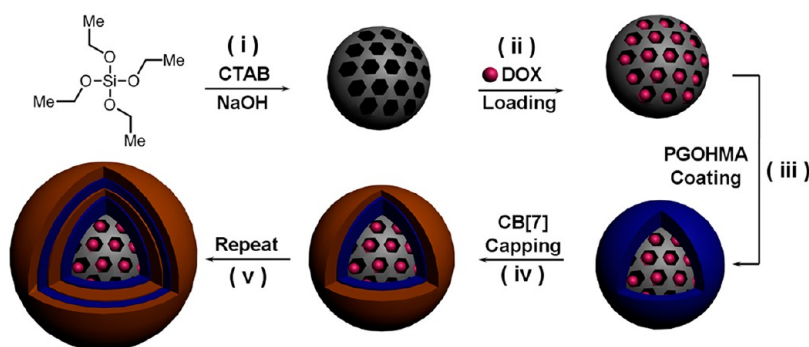
[a](i) Template activation for 30 min or 2 h, followed by addition of TEOS, heating at 80 °C, 2 h. (ii) DOX (0.5 mM) loading. (iii) EDA-PGOHMA capping and then washing with PBS buffer. (iv) CB[7] Capping and then washing with PBS buffer. (v) Repeat (iii) and (iv).
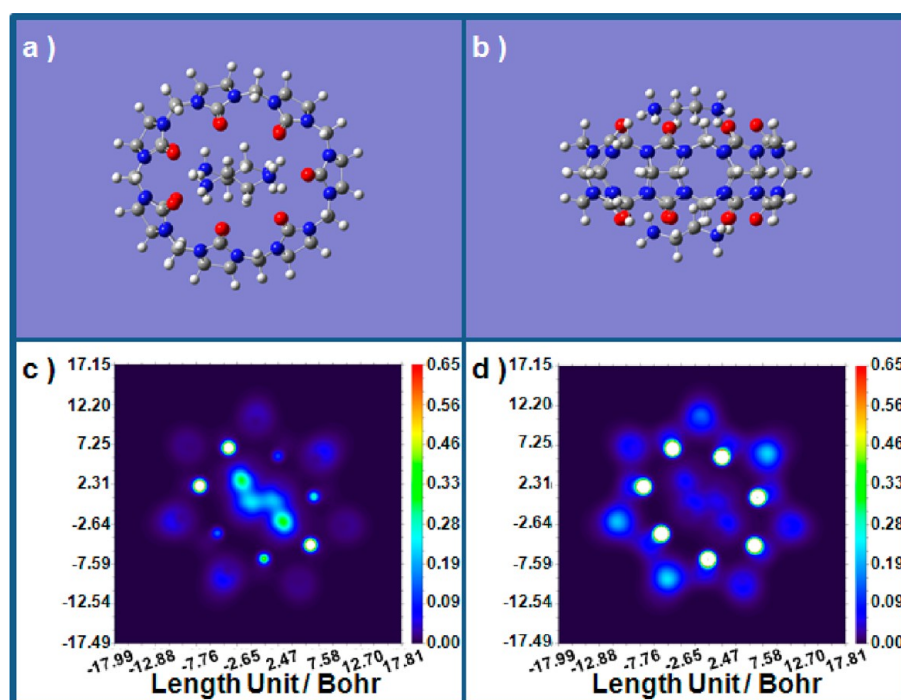
Figure 6. Binding mode (a, b) of CB[7] and EDA and electron density of the complex (c, d) between CB[7] and EDA.

sonication for 2 min without affecting the stability of the system. For efficient cellular uptake of nanoparticles, it is desirable that the LbL-MSNs remain dispersed and do not aggregate in solution. The observed aggregation might be caused by interparticle hydrogen-bonding interactions. Cellular uptake of the PI-loaded LbL-MSNs was investigated by confocal laser scanning microscopy (CLSM). Figure 7 shows that MDA-MB-231 cancer cells effectively endocytosed[81] LbL-MSN-1 and LbL-MSN-2 within 2 h, in agreement with previous MSN studies.[36] This action was followed by PI release to the nucleus after 24 h, as shown by the colocalization experiment with the DAPI nuclear stain. Compared with normal cells, there are a series of different microstructural features and physicochemical properties of cancer cells, such as vascular abnormalities, weak acidity, abnormal temperature gradients, overexpressed proteins and enzymes, and hypoxia. Meanwhile, intracellular microenvironments play a more important role on cellular uptake of nanoparticles within cancer cells. Except acidic pH inside endosomes and lysosomes, it also includes reductive microenvironments because of the presence of high level cysteine or glutathione (GSH) in the cytoplasm and endolysosomes, oxidative microenvironment in mitochondria with a high concentration of H_2O_2, and various biomolecules and metabolites within cytoplasm and subcellular organelles. In other words, major mechanisms that lead to tumor acidity might include the production of lactic acid and hydrolysis of ATP in hypoxic regions of tumors. Further reduction in pH may be achieved in some tumors by administration of glucose and by drugs such as hydralazine which will modify the relative blood flow to tumors and normal tissues.[82] The PI release is most likely triggered by the highly acidic endosomal compartments characteristic of cancerous cells as shown in other pH-activated delivery systems.[29] In addition, no evident cytotoxicity was observed on the microscope stage even after 3 days, indicating the good biocompatibility of LbL-MSN materials. These results demonstrate that PI-loaded LbL-MSNs (i) can be internalized by cells, (ii) can be easily detected by confocal microscopy, and (iii) reside in the cytoplasm of the cells without marked nuclear localization.

Macrophages are dedicated human immune cells, playing the role of identifying and defeating foreign substances and other debris in the body. However, it depends on the surface feature of these dangerous materials. Macrophages can only swallow the materials that are more hydrophobic than itself.[83] Therefore, hydrophilic poly(ethylene glycol) (PEG) has been widely used to coat on the surface of a drug delivery system to reduce the phagocytosis of macrophages. In our current design, a small amount of PEG or CB[7] was added into the PI-loaded LbL-MSNs. The mixture was dispersed in a medium and placed in a cell culture plate. After several hours, cellular uptake of the mixtures was investigated by CLSM and compared with PI-loaded LbL-MSNs, as shown in Figure 8. Obviously, fewer LbL-MSNs were endocytosed into macrophages with a few percentage points of PEG or CB[7], probably due to the enhanced surface hydrophilicity of LbL-MSNs induced by PEG and CB[7]. It is reasonable and appreciable that macrophages did not identify LbL-MSNs as dangerous materials upon addition of a small amount of PEG or CB[7], especially PEG. In addition, the swallowing mechanism of macrophages is so different with cancerous cells (EPR effect).[84] Therefore, addition of PEG or CB[7] was supposed to have no effect on cancer treatment.

To determine whether the LbL-MSNs are able to not only transport the anticancer drugs into the cancer cells but also accomplish therapeutic actions, a homogeneous suspension of the DOX-loaded LbL-MSNs in the cell culture medium has been used to cultivate HeLa cells, in comparison with fibroblast L929 cells. A CCK-8 assay was used for quantitative testing of the viability of HeLa cells for DOX-loaded LbL-MSN-1, DOX-loaded LbL-MSN-2, and DOX (Figure 9). The cell viability decreased with an increasing concentration of DOX. Compared with pure DOX, the lower cytotoxicity of DOX-loaded LbL-
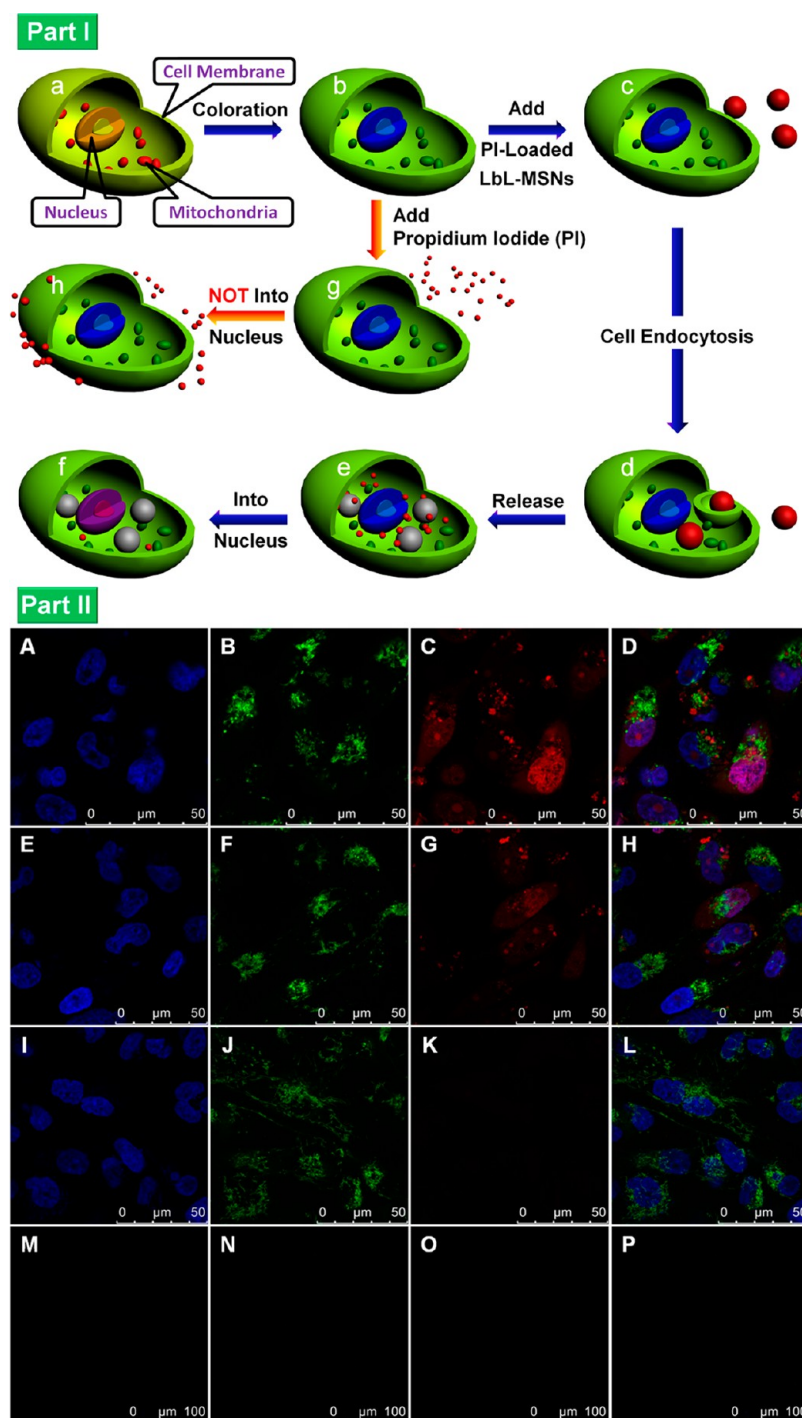
Figure 7. Cellular uptake experiment in MDA-MB-231 cancer cells. Part I: (a) Cell model: Only nucleus and mitochondria were shown in this model. (b) Nucleus and mitochondria were colored by fluorescent dyes. (c) PI-loaded LbL-MSNs were added into the medium containing cells. (d) PI-loaded LbL-MSNs got into cells by cell endocytosis. (e) PI molecules were released because of the lower pH value of cancer cells. (f) PI molecules entered into nucleus, which was colored. (g) PI solution was added into the cell-contained medium immediately. (h) The nucleus was not colored because PI cannot enter into cells without encapsulation within nanoparticles. Part II: LbL-MSNs were loaded with plasma-membrane-impermeable PI molecules and incubated with the cells for 24 h. The following cellular organelles were stained selectively using standard protocols: mitochondria (with MitoTracker Green FM, 50 nM) and nuclei (with DAPI, 300 nM). (A, E, I, M) Nuclei (Blue channel, λ_{ex} = 405 nm, λ_{em} = 445 ± 15 nm). (B, F, J, N) Mitochondria (Green channel, λ_{ex} = 488 nm, λ_{em} = 516 ± 15 nm). (C) PI-loaded LbL-MSN-1 (Red channel, λ_{ex} = 561 nm, λ_{em} = 617 ± 15 nm). (G) PI-loaded LbL-MSN-2 (Red channel, λ_{ex} = 561 nm, λ_{em} = 617 ± 15 nm). (D) An overlay of (A)−(C). (H) An overlay of (E)−(G). (I, J, K, L) Free PI stained cells as a control experiment, which shows that PI did not penetrate the cell membrane and was readily washed away before cell imaging experiment. (M, N, O, P) Control experiment without stained cells shows that no fluorescent signals could be detected under the same experimental settings. The multicolor confocal microscopic images show that PI-loaded LbL-MSN-1 and PI-loaded LbL-MSN-2 have been localized into the cells after 4 h. The appearance of nuclear costaining (violet) indicates the release of PI dye from the nanocarriers of LbL-MSN-1 (D) and LbL-MSN-2 (H) to the nucleus.
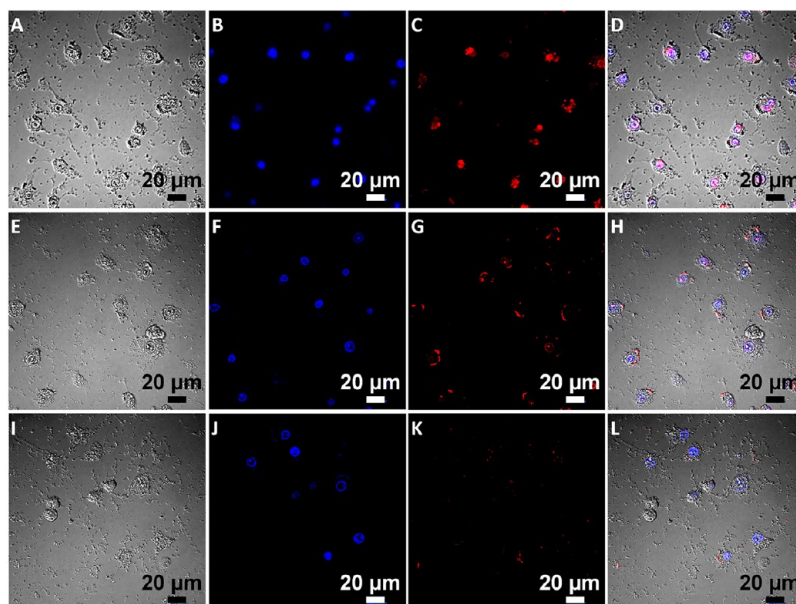
Figure 8. Cellular uptake experiment using macrophages. LbL-MSNs were loaded with plasma-membrane-impermeable PI molecules and incubated with the cells for 3 h. The following cellular nuclei were stained using DAPI (300 nM). (A, E, I) Cellular contours. (B, F, J) Nuclei (Blue channel, λ_{ex} = 405 nm, λ_{em} = 445 ± 15 nm). (C) PI-loaded LbL-MSN-1 (Red channel, λ_{ex} = 561 nm, λ_{em} = 617 ± 15 nm). (G) PI-loaded LbL-MSN-1 with 10% of CB[7] (Red channel, λ_{ex} = 561 nm, λ_{em} = 617 ± 15 nm). (K) PI-loaded LbL-MSN-1 with 10% of PEG (Red channel, λ_{ex} = 561 nm, λ_{em} = 617 ± 15 nm). (D) An overlay of (A)−(C). (H) An overlay of (E)−(G). The multicolor confocal microscopic images show that very few LbL-MSNs were endocytosed into macrophage with the employment of a few percentage points of PEG or CB[7].
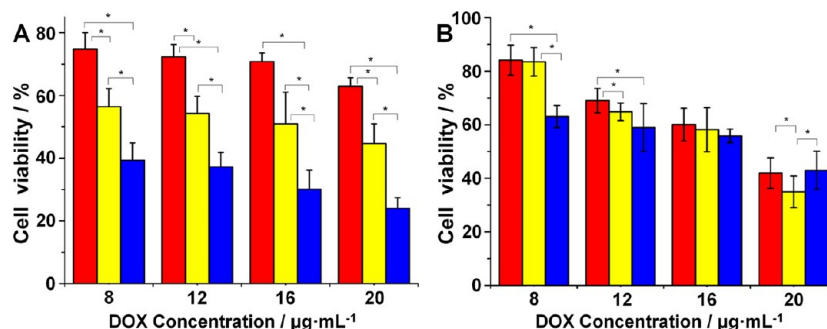

Figure 9. In vitro cell-growth inhibition assay for fibroblast L929 cell line (A) and HeLa cell line (B) obtained by adding DOX-loaded LbL-MSN-1 (red), DOX-loaded LbL-MSN-2 (yellow), and DOX (blue). Asterisk (*) indicates significant differences ($p < 0.05$) between every two groups. Results are shown as mean ± standard deviation (n = 4).

MSNs was mainly a result of the sustained drug release from the materials. Consequently, the cell viability against fibroblast L929 cells was significantly increased for DOX-loaded LbL-MSNs, as compared with DOX itself, indicating that loading of the drug into the LbL-MSNs reduced the drug side effects efficiently. The higher cell viability for HeLa cells compared to that of L929 cells is probably due to the fast reproduction ability of HeLa cells. Significantly, for HeLa cells, the cell viability of DOX-loaded LbL-MSNs was higher than that of pure DOX at lower DOX concentrations. However, DOX-loaded LbL-MSN-2 is more toxic than DOX-loaded LbL-MSN-1 at concentrations of 12 and 20 μg/mL (Figure 9).

Evaluation of the Treatment Efficacy by Caspase-3 Test. Caspase family plays a significant role in the process of mediated apoptosis.[85] Among them, caspase-3 (CPP32) is the key executive molecule because it can perform its functions in many ways of apoptosis signaling. In normal conditions, CPP32 exists in cytoplasm almost inactively in the form of pro-caspase-3 (pro-CPP32). During the early stage of apoptosis, pro-CPP32

can be activated into CPP32, which can crack the corresponding substrates from nucleus and cytoplasm and result in apoptosis. According to this principle, N-acetyl-Asp-Glu-Val-Asp-7-amido-4-trifluoromethylcoumarin (Ac-DEVD-AFC)[86] was used for detecting caspase-3 to evaluate treatment efficacy. The experimental results showed that CPP32 activities rise with increased concentrations of DOX, which illustrated that LbL-MSNs act on the HeLa cells to cause the cell death by way of apoptosis (Figure 10).

In Vivo Tumor-Growth Inhibition Experiments. The anticancer activity and side effects of DOX and DOX-loaded LbL-MSNs could be distinguished visually from the physical appearance of the mice in terms of tumor size and body weight. To validate the practical application of DOX-loaded LbL-MSNs in cancer treatment, in vivo anticancer experiments were carried out on a BALB/c nude mice model that contained HeLa cancer cells.[87] As shown in Figure 11, mice with tumors were divided into three groups, one of which was untreated (the control) and two of which were injected with DOX or DOX-loaded
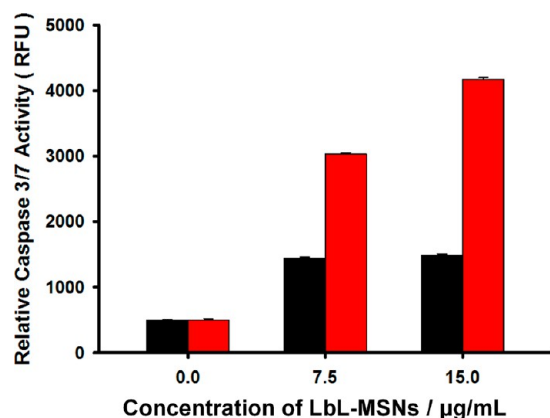
Figure 10. In vitro HeLa cell assay for relative caspase-3/7 activity: LbL-MSN-1 (black); LbL-MSN-2 (red).

LbL-MSNs by the tail vein. The tumor volumes of the mice in the untreated group increased steadily over the entire experimental period. Owing to the good antitumor effect of DOX, tumor growth was suppressed in the DOX group, with a tumor-growth inhibition of 41% by day 28. In sharp contrast, DOX-loaded MSNs showed a much higher tumor-growth inhibition of 63% on day 28. The results indicated that the DOX-loaded LbL-MSNs have great potential to serve as effective anticancer drug nanocarriers.

CONCLUSIONS

In conclusion, two types of MSNs coated with LbL assemblies have been prepared by supramolecular self-assembly, based on the noncovalent bonding interactions between BA-PGOHMAs and CB[7] under neutral conditions, and have shown to be able to trap cargo. Release of the cargo molecules, be they a drug (DOX) or a biocompatible dye (PI), can be achieved by lowering the pH or by adding AH for CB[7] host. Among all the employed BA-PGOHMAs, the EDA-PGOHMA-based drug delivery system has displayed the best performance in terms of loading capacity and release efficiency. This better performance might be related to a 1:2 complexation between CB[7] and the EDA linker, which would effectively enhance the supramolecular gluing by the CB[7] macrocycle. This hypothesis is also supported by the theoretical modeling. The good biocompatibility and efficient stimuli-responsive drug release ability of the present LbL-coated MSNs hybrid nanomaterials based on EDA-PGOHMAs and CB[7]s, both in vitro and in vivo, opens up an alternative new avenue for the in vivo controlled release of drugs in biomedical applications.

EXPERIMENTAL SECTION

Materials. Tetraethoxysilane (TEOS), 1,3,5-trimethylbenzene, 3-isocyanatopropyl triethoxysilane (IPTES), cetyltrimethylammonium bromide (CTAB), adamantaneamine hydrochloride (AH), 2-bromoisobutyryl bromide, glycidyl methacrylate (GMA), ethanediamine (EDA), 1,4-butanediamine (BDA), 1,6-hexamethylenediamine (HDA), and 2,2′-bipyridine were purchased from the Aladdin Reagent Co., Ltd. DOX was purchased from Beijing Huafeng United Technology Co., Ltd. CuBr was obtained from J&K Co., Ltd. Cell Counting Kit-8 (CCK-8) was obtained from Dojindo (Beijing, China). Propidium iodide (PI) was purchased from Sigma-Aldrich. All the starting materials and reagents were used as received. A series of phosphate buffers (PBS buffers) were prepared according to Appendix XV of the Chinese Pharmacopeia (Second Part, 2010 Edition). CB[7] was synthesized according to a procedure reported by Day.[88] Unless otherwise noted, all reactions were performed under anitrogen atmosphere and in dry solvents.
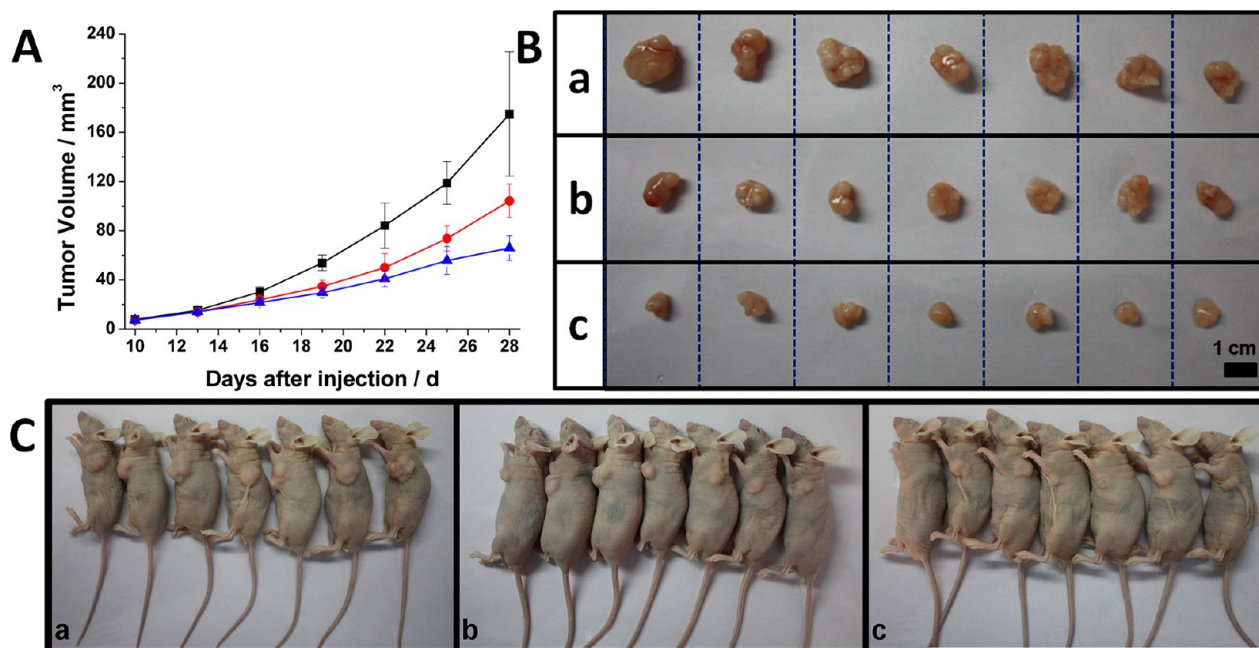

Figure 11. Tumor growth curves (A) for BALB/c nude mice with HeLa cancer cells treated with DOX-loaded LbL-MSNs (blue), DOX (red), and blank control (black). The injected dose was normalized to be 4 mg/kg DOX. The images of tumor volume (B) for BALB/c nude mice with HeLa cancer cells treated with blank control (a), DOX (b), and DOX-loaded LbL-MSNs (c). Nude mice images (C) of mice treated with (a) blank control, (b) DOX, and (c) DOX-loaded LbL-MSNs.

Methods. Scanning electron microscope (SEM) images were collected on a JEOL JSM 6700F instrument. Au coating of nanoparticles used for imaging was carried out by sputtering for 90 s. Transmission electron microscopy (TEM) images were collected on a JEM-2100F instrument, employing an accelerating voltage of 200 kV. Fourier transform infrared (FT-IR) spectra were recorded on a Bruker Vertex 80 V spectrometer. Thermogravimetric analysis (TGA) was carried out on a TA Q500 instrument with a heating program consisting of a heating rate of 10 °C/min from 308 to 1173 K. ^{1}H NMR spectra were recorded on a Bruker 500 MHz NMR spectrometer. Powder X-ray diffraction (XRD) measurements were carried out using a Rigaku SmartLab III powder diffractometer. The radiation source was copper (Kα = 1.39225 Å). N$_2$ adsorption and desorption isotherms were obtained using a Micromeritics Gemini instrument. Specific surface areas were calculated from the adsorption data in the low-pressure range using the Brunauer−Emmett−Teller (BET) model. Pore sizes were determined following the Barrett−Joyner−Halenda (BJH) method. Controlled release profiles were obtained via UV−vis spectroscopy using a Shimadzu UV-2550 spectrophotometer.

Preparation of Traditional MSNs (MSN-1). Generally, CTAB (1.0 g), 2 M NaOH (aq, 3.5 mL), and H$_2$O (240 mL) were mixed and heated at 80 °C for 30 min to activate the template. After the reaction mixture turned into a clear surfactant solution, TEOS (5.0 mL) and IPTES (0.6 mL) were added sequentially and rapidly via injection. A white precipitate was obtained after 15 min of vigorous stirring. The reaction temperature was maintained at 80 °C for another 2 h. The resulting precipitate was isolated by hot filtration, washed with 200 mL of H$_2$O and MeOH, and dried under vacuum overnight to obtain the as-synthesized materials. To remove the templates and so generate the porous materials, acid extraction on the as-synthesized materials (1.0 g) was performed in MeOH (100 mL) with concentrated HCl (1.0 mL) at 60 °C for 6 h. Finally, the traditional carboxyl-modified MSN (MSN-1) products were filtered and washed with H$_2$O and MeOH, before being dried under vacuum overnight. MSN-1 was characterized by SEM, TEM, XRD, FT-IR, BET, and BJH.

Preparation of Swollen MSNs (MSN-2). A method similar to the synthesis of MSN-1 was used to prepare MSN-2. CTAB (1.0 g) was dissolved in a mixture of H$_2$O (480 mL) and 2 M NaOH (aq, 3.5 mL). Mesitylene (7.0 mL) was added to the above solution. The mixture was stirred vigorously at 80 °C for 2 h. TEOS (5.0 mL) was then added dropwise to the solution, which was stirred vigorously at 80 °C for another 2 h to give a white precipitate. The product was isolated by filtration, washed with excess of MeOH, and dried under vacuum overnight. A suspension of the as-synthesized material (1.0 g) in MeOH (100 mL) was stirred for 6 h at 50 °C in the presence of concentrated HCl (0.75 mL) to remove the template. The resulting solid product was then isolated by filtration and dried under vacuum at room temperature overnight. MSN-2 was characterized by SEM, TEM, XRD, FT-IR, BET, and BJH.

Synthesis of 5-Arm PGMA and 5-Arm BA-PGOHMAs. 5-Arm poly(glycidyl methacrylate) (PGMA) was synthesized by atom-transfer radical polymerization (ATRP) using the 5-arm ATRP initiator, 1,2,3,4,6-penta-O-isobutyryl bromide-α-D-glucose. See the Supporting Information for details. The molecular weights of the synthesized polymers were determined by gel permeation chromatography (Figure S1).

The resulting 5-arm PGOHMA was then modified with different amines by ring openings of the epoxides (Scheme S2).

DOX Loading and LbL Self-assembly. Loading of the nanopores of MSNs (20 mg) with DOX was carried out by soaking both kinds of MSNs in an aqueous solution of DOX (0.5 mM in PBS, 10 mL, pH = 7.4) for 5 h at room temperature. Then BA-PGOHMA (18 mg) was dissolved in PBS (pH = 7.4, 1 mL) before added to the loading solution. Subsequently, the mixture was sonicated and stirred for 15 min. The precipitate was centrifuged and redispersed into another batch of fresh PBS buffer. Meanwhile, CB[7] (12 mg) was dissolved in PBS (pH = 7.4, 1 mL) and added to the mixture, following the sonication and stirring. The procedure was repeated once. Finally, the as-made materials were washed with PBS (pH = 7.4) three times and then lyophilized.

Controlled Release Experiments by Changing pH Values. Controlled release experiments were carried out at different pH values. The LbL-MSNs (5 mg) were dispersed in 1 mL of PBS (pH = 7.4, 5, and 2, respectively) and dialyzed against their corresponding buffer solutions (20 mL) in capped beakers under stirring at 37 °C. At every designated interval, buffer solutions (4 mL) in the beaker were taken out and fresh buffer solution (4 mL) was replenished to keep a constant volume. The amount of DOX released into the buffer solution was analyzed using a UV−vis spectrophotometer at a wavelength of 498 nm. The concentration of DOX released from the materials was expressed as a percentage of the total DOX available and plotted as a function of time. The cumulative DOX release was calculated through the equation below (eq 7):

$$\text{cumulative DOX release } (\%) = M_t/M_\infty \times 100\% \tag{7}$$

where M_t is the amount of drug (DOX) released from materials at time t and M_∞ is the amount of drug released from the materials at time infinity. The spectroscopic setup for the controlled release experiments is shown in Figure S4 in the Supporting Information.

Controlled Release Experiments by Adding AH. LbL-MSNs (5 mg) were dispersed in H$_2$O (1.0 mL) and dialyzed against AH solutions (20 mL, 0.1 M) in capped beakers at 37 °C. At designated intervals, the solution of AH (4 mL) in the beaker was taken out and a corresponding fresh solution (4 mL) was replenished to keep a constant volume. The spectroscopic setup was the same (Figure S4). Unless otherwise noted, LbL-MSNs stands for LbL-MSN systems based on EDA-PGOHMA.

Cell Culture. The human breast cancer cell line MDA-MB-231 was cultured in RPMI medium (Sigma) supplemented with 10% fetal bovine serum (FBS; Gibco) in a humidified atmosphere of 5% CO$_2$ in air at 37 °C. The media were changed every 3 days, and the cells were passaged by trypsinization before confluency. The method for preparing the PI-loaded LbL-MSNs was the same as that for DOX-loaded LbL-MSNs. Loading PI into the nanopores of MSNs (10 mg) was carried out by soaking the two kinds of MSNs in PBS buffer of PI (1 mg/mL) overnight at room temperature. Then EDA-PGOHMA (10 mg) was dissolved in PBS buffer (0.2 mL) and added into the loading solution. Subsequently, the mixture was sonicated and stirred for 10 min. The precipitate was centrifuged and redispersed into another batch of fresh PBS buffer. Meanwhile, CB[7] (10 mg) was dissolved in PBS buffer (0.2 mL) and added to the mixture, following sonication and stirring. The procedure was repeated once. Finally, the as-made

materials were washed with PBS, suspended in H_2O, and then lyophilized to dryness.

Live Cell Imaging of Cancer Cells. The cellular uptake of the LbL-MSNs by the human breast cancer cell line MDA-MB-231 was confirmed by fluorescence microscopy. Imaging was performed using an inverted confocal microscope (Leica TCS SP5 II LSCM) equipped with a diode (405 nm), Ar (457, 467, 488, and 514 nm), solid-state DPSS (561 nm), and HeNe (633 nm) excitation laser. This system comprises a tandem scanner that has both a standard scanner (low speed, resolution up to 8K × 8K) and a resonant scanner (high speed, resolution up to 1K × 1K). In addition to standard PMTs, this system has HyD detectors (GaAsP) that combine high sensitivity and low noise. The fluorescence spectra from cell cultures were obtained on the microscope with ca. 10 nm of resolution. Water immersion at 63× objective (NA = 1.20) was used in all measurements, unless otherwise stated. For imaging, cells were seeded (5000 cells per well) in 0.5 mL of culture medium in an untreated tissue culture dish with a cover glass bottom (WPI) and allowed to attach for 24 h. The culture media was replaced with the medium containing the PI-loaded LbL-MSNs (0.1 mg/mL) and incubated for 2−4 h. Following incubation, the chambers were washed with phosphate buffered saline (PBS) and RPMI medium, prior to imaging to remove the LbL-MSNs that did not enter the cells. For the multicolor fluorescent experiments, the same cells were incubated with 300 nM DAPI nuclear stain (Invitrogen, λ_{ex} = 405 nm) and 50 nM MitoTracker Green FM mitochondrial stain (Invitrogen, λ_{ex} = 488 nm) for 30 min, before being monitored by fluorescence microscopy. No background fluorescence of cells was detected with the microscope settings employed.

Live Cell Imaging of Macrophages. Macrophage cells were cultured in RPMI-1640 medium (Invitrogen) containing 10% fetal bovine serum, penicillin (100 units/mL), streptomycin (100 mg/mL), and 5% CO_2 at 37 °C. One day before experiment, cell suspensions were plated at a density of 1.0×10^4 cells/mL on 35 mm diameter round glass coverslips. Then the cells were incubated with LbL-MSNs (0.1 mg/mL), preloaded with plasma-membrane-impermeable PI molecules, for 3 h at 37 °C in 5% CO_2 and washed three times with PBS buffer (0.10 M, pH 7.4) before imaging. The cellular nuclei were stained using DAPI (300 nM). Fluorescent images were acquired on a Nikon A1 confocal laser-scanning microscope with a 60× objective lens.

Cell Viability Assays. A HeLa or fibroblast L929 cells suspension (100 μL) was added into 96-well microplates, with 5000 cells immersed in the complete growth medium per well, cultivated in a humidified 5% CO_2 atmosphere at 37 °C for 24 h to allow cells to attach. Subsequently, LbL-MSN samples at different concentrations in PBS solution (pH 7.4) were added to 96-well plates, followed by incubation for 24 h. Then a CCK-8 solution was added to the 96-well plates at 10 μL/well and incubated for 3 h. The resulting solutions were analyzed at 480 nm by means of a plate reader (BIO-TEK Instruments Inc., EL311S, Winooski, VT). This process was repeated 8 times in parallel. The results are expressed as the relative cell viability (%) with respect to a blank group only with a culture medium.

Caspase-3 Test. HeLa cells were treated with G-Rh2 (7.5 μg/mL) in serum-free media for indicated time periods and then were harvested. Fifty micrograms of cell lysates were incubated with 200 nM Ac-DEVD-AFC in a reaction buffer containing 20 mM HEPES, pH 7.4, 100 mM NaCl, 10 mM DTT, 0.1% CHAPS, and 10% sucrose at 37 °C for 1 h. The reaction was monitored by fluorescence emission at 535 nm and excitation at 405 nm.

In Vivo Studies. Four-week-old BALB/c female nude mice were purchased from Institute of Laboratory Animal Sciences, CAMS & PUMC (P.R. China). The HeLa tumor models were generated by subcutaneous injection of (2×10^6) HeLa cells in RPMI-1640 medium into the oxter of each mouse. When the tumor volume reached 7 mm^3 (ca. 10 days after tumor implantation), the mice were divided into three groups (7 mice per group). Two of the groups of mice were injected with DOX or DOX-loaded LbL-MSNs through the tail vein every 3 days. The DOX doses were set at 4 mg/kg. The tumor volumes (V) were measured by using a caliper and calculated by using the following formula (eqs 8):

$$V = 0.5 \times (\text{tumor length}) \times (\text{tumor width})^2 \tag{8}$$

Statistics Analysis. Significant differences in cell viability between any two groups were evaluated using Student's t test.

■ ASSOCIATED CONTENT

ⓢ Supporting Information

Synthesis and GPC of 5-arm PGMA and BA-PGOHMAs, ^{1}H NMR of HDA-PGOHMA, SEM, TGA, more in vitro and in vivo experiments, and spectroscopic setup for controlled release experiments. This material is available free of charge via the Internet at http://pubs.acs.org.

■ AUTHOR INFORMATION

Corresponding Authors
*E-mail: ywyang@jlu.edu.cn (Y.W.Y.).
*E-mail: ghhigher@hotmail.com (H.G.).

Notes
The authors declare no competing financial interest.

■ ACKNOWLEDGMENTS

■ REFERENCES

(1) Descalzo, A. B.; Martinez-Máñez, R.; Sancenón, F.; Hoffmann, K.; Rurack, K. Angew. Chem., Int. Ed. 2006, 45, 5924−5948.
(2) Jiang, S.; Cheng, R.; Wang, X.; Xue, T.; Liu, Y.; Nel, A.; Huang, Y.; Duan, X. Nat. Commun. 2013, 4, 2225 DOI: 10.1038/ncomms3225.
(3) Meng, H.; Yang, S.; Li, Z.; Xia, T.; Chen, J.; Ji, Z.; Zhang, H.; Wang, X.; Lin, S.; Huang, C.; et al. ACS Nano 2011, 5, 4434−4447.
(4) Meng, H.; Liong, M.; Xia, T.; Li, Z.; Ji, Z.; Zink, J. I.; Nel, A. E. ACS Nano 2010, 4, 4539−4550.
(5) Meng, H.; Mai, W. X.; Zhang, H.; Xue, M.; Xia, T.; Lin, S.; Wang, X.; Zhao, Y.; Ji, Z.; Zink, J. I.; et al. ACS Nano 2013, 7, 994−1005.

(6) Lu, J.; Liong, M.; Sherman, S.; Xia, T.; Kovochich, M.; Nel, A. E.; Zink, J. I.; Tamanoi, F. *Nanobiotechnology* **2007**, *3*, 89−95.

(7) Collins, L.; Separovic, F.; Parker, A. L.; Fabre, a. J. W.; Gehman, J. D.; Eckley, L.; Perugini, M. A. *ACS Nano* **2010**, *4*, 2856−2864.

(8) Yang, Y.-W. *Med. Chem. Commun.* **2011**, *2*, 1033−1049.

(9) Borisova, D.; Möhwald, H.; Shchukin, D. G. *ACS Nano* **2011**, *5*, 1939−1946.

(10) Zheng, Z.; Huang, X.; Schenderlein, M.; Borisova, D.; Cao, R.; Möhwald, H.; Shchukin, D. *Adv. Funct. Mater.* **2013**, *23*, 3307−3314.

(11) Uhrich, K. E.; Cannizzaro, S. M.; Langer, R. S.; Shakesheff, K. M. *Chem. Rev.* **1999**, *99*, 3181−3198.

(12) Vallet-Regi, M.; Rámila, A.; Real, R. P. d.; Pérez-Pariente, J. *Chem. Mater.* **2001**, *13*, 308−311.

(13) Yang, Y.-W.; Sun, Y.-L.; Song, N. *Acc. Chem. Res.* **2014**, *47*, 1950−1960.

(14) Li, Z.; Barnes, J. C.; Bosoy, A.; Stoddart, J. F.; Zink, J. I. *Chem. Soc. Rev.* **2012**, *41*, 2590−2605.

(15) Li, D.; Liu, J.; Kwok, R. T.; Liang, Z.; Tang, B. Z.; Yu, J. *Chem. Commun.* **2012**, *48*, 7167−7169.

(16) Mal, N. K.; Fujiwara, M.; Tanaka, Y. *Nature* **2003**, *421*, 350−353.

(17) Lai, C.-Y.; Trewyn, B. G.; Jeftinija, D. M.; Jeftinija, K.; Xu, S.; Jeftinija, S.; Lin, V. S.-Y. *J. Am. Chem. Soc.* **2003**, *125*, 4451−4459.

(18) Hernandez, R.; Tseng, H.-R.; Wong, J. W.; Stoddart, J. F.; Zink, J. I. *J. Am. Chem. Soc.* **2004**, *126*, 3370−3371.

(19) Casasús, R.; Marcos, M. D.; Martínez-Máñez, R.; Ros-Lis, J.; Soto, J.; Villaescusa, L. A.; Amorós, P.; Beltrán, D.; Guillem, C.; Latorre, J. *J. Am. Chem. Soc.* **2004**, *126*, 8612−8613.

(20) Giri, S.; Trewyn, B. G.; Stellmaker, M. P.; Lin, V. S. *Angew. Chem., Int. Ed.* **2005**, *44*, 5038−5044.

(21) Muhammad, F.; Guo, M.; Qi, W.; Sun, F.; Wang, A.; Guo, Y.; Zhu, G. *J. Am. Chem. Soc.* **2011**, *133*, 8778−8781.

(22) Zhu, Y.; Shi, J.; Shen, W.; Dong, X.; Feng, J.; Ruan, M.; Li, Y. *Angew. Chem., Int. Ed.* **2005**, *44*, 5083−5087.

(23) Wang, C.; Li, Z.; Cao, D.; Zhao, Y.-L.; Gaines, J. W.; Bozdemir, O. A.; Ambrogio, M. W.; Frasconi, M.; Botros, Y. Y.; Zink, J. I.; et al. *Angew. Chem., Int. Ed.* **2012**, *51*, 5460−5465.

(24) Angelos, S.; Yang, Y.-W.; Khashab, N. M.; Stoddart, J. F.; Zink, J. I. *J. Am. Chem. Soc.* **2009**, *131*, 11344−11346.

(25) Ferris, D. P.; Zhao, Y.-L.; Khashab, N. M.; Khatib, H. A.; Stoddart, J. F.; Zink, J. I. *J. Am. Chem. Soc.* **2009**, *131*, 1686−1688.

(26) Sun, Y.-L.; Yang, B.-J.; Zhang, S. X.-A.; Yang, Y.-W. *Chem.—Eur. J.* **2012**, *18*, 9212−9216.

(27) Angelos, S.; Yang, Y.-W.; Patel, K.; Stoddart, J. F.; Zink, J. I. *Angew. Chem., Int. Ed.* **2008**, *47*, 2222−2226.

(28) Angelos, S.; Khashab, N. M.; Yang, Y.-W.; Trabolsi, A.; Khatib, H. A.; Stoddart, J. F.; Zink, J. I. *J. Am. Chem. Soc.* **2009**, *131*, 12912−12914.

(29) Meng, H.; Xue, M.; Xia, T.; Zhao, Y.-L.; Tamanoi, F.; Stoddart, J. F.; Zink, J. I.; Nel, A. E. *J. Am. Chem. Soc.* **2010**, *132*, 12690−12697.

(30) Zhao, Y.-L.; Li, Z.; Kabehie, S.; Botros, Y. Y.; Stoddart, J. F.; Zink, J. I. *J. Am. Chem. Soc.* **2010**, *132*, 13016−13025.

(31) Croissant, J.; Zink, J. I. *J. Am. Chem. Soc.* **2012**, *134*, 7628−7631.

(32) Zhou, Y.; Tan, L.-L.; Li, Q.-L.; Qiu, X.-L.; Qi, A.-D.; Tao, Y.-C.; Yang, Y.-W. *Chem.—Eur. J.* **2014**, *20*, 2998−3004.

(33) Patel, K.; Angelos, S.; Dichtel, W. R.; Coskun, A.; Yang, Y.-W.; Zink, J. I.; Stoddart, J. F. *J. Am. Chem. Soc.* **2008**, *130*, 2382−2383.

(34) Sun, Y.-L.; Yang, Y.-W.; Chen, D.-X.; Wang, G.; Zhou, Y.; Wang, C.-Y.; Stoddart, J. F. *Small* **2013**, *9*, 3224−3229.

(35) Sun, Y.-L.; Zhou, Y.; Li, Q.-L.; Yang, Y.-W. *Chem. Commun.* **2013**, *49*, 9033−9035.

(36) Lu, J.; Choi, E.; Tamanoi, F.; Zink, J. I. *Small* **2008**, *4*, 421−426.

(37) Tarn, D.; Ferris, D. P.; Barnes, J. C.; Ambrogio, M. W.; Stoddart, J. F.; Zink, J. I. *Nanoscale* **2014**, *6*, 3335−3343.

(38) Li, Q.-L.; Wang, L.; Qiu, X.-L.; Sun, Y.-L.; Wang, P.-X.; Liu, Y.; Li, F.; Qi, A.-D.; Gao, H.; Yang, Y.-W. *Polym. Chem.* **2014**, *5*, 3389−3395.

(39) Croissant, J.; Maynadier, M.; Gallud, A.; N'Dongo, H. P.; Nyalosaso, J. L.; Derrien, G.; Charnay, C.; Durand, J.-O.; Raehm, L.; Serein-Spirau, F.; et al. *Angew. Chem., Int. Ed.* **2013**, *52*, 13813−13817.

(40) Li, H.; Tan, L.-L.; Jia, P.; Li, Q.-L.; Sun, Y.-L.; Zhang, L.; Ning, Y.-Q.; Yu, J.; Yang, Y.-W. *Chem. Sci.* **2014**, *5*, 2804−2808.

(41) Chen, L.; Wang, W.; Su, B.; Wen, Y.; Li, C.; Zhou, Y.; Li, M.; Shi, X.; Du, H.; Song, Y.; et al. *ACS Nano* **2014**, *8*, 744−751.

(42) Dong, J.; Xue, M.; Zink, J. I. *Nanoscale* **2013**, *5*, 10300−10306.

(43) Tarn, D.; Xue, M.; Zink, J. I. *Inorg. Chem.* **2013**, *52*, 2044−2049.

(44) Porta, F.; Lamers, G. E. M.; Morrhayim, J.; Chatzopoulou, A.; Schaaf, M.; Dulk, H. d.; Backendorf, C.; Zink, J. I.; Kros, A. *Adv. Healthcare Mater.* **2013**, *2*, 281−286.

(45) Ma, Y.; Zhou, L.; Zheng, H.; Xing, L.; Li, C.; Cui, J.; Che, S. *J. Mater. Chem.* **2011**, *21*, 9483−9486.

(46) Xing, L.; Zheng, H.; Cao, Y.; Che, S. *Adv. Mater.* **2012**, *24*, 6433−6437.

(47) Li, Q.-L.; Gu, W.-X.; Gao, H.; Yang, Y.-W. *Chem. Commun.* **2014**, *50*, 13201−13215.

(48) Gao, H.; Lu, X.; Ma, Y.; Yang, Y.; Li, J.; Wu, G.; Wang, Y.; Fan, Y.; Ma, J. *Soft Matter* **2011**, *7*, 9239−9247.

(49) Gao, H.; Elsabahy, M.; Giger, E. V.; Ma, J.; Prud'homme, R. E.; Leroux, J. C. *J. Controlled Release* **2011**, *152*, 142−143.

(50) Ma, Y.; Gao, H.; Gu, W.; Yang, Y.-W.; Wang, Y.; Fan, Y.; Wu, G.; Ma, J. *Eur. J. Pharm. Sci.* **2012**, *45*, 65−72.

(51) Liang, Z.; Wu, X.; Yang, Y.-W.; Li, C.; Wu, G.; Gao, H. *Polym. Chem.* **2013**, *4*, 3514−3523.

(52) Sun, Y.; Gao, H.; Yang, Y.-W.; Wang, A.; Wu, G.; Wang, Y.; Fan, Y.; Ma, J. *J. Biomed. Mater. Res., Part A* **2013**, *101A*, 2164−2173.

(53) Li, C.; Yang, Y.-W.; Liang, Z.; Wu, G.; Gao, H. *Polym. Chem.* **2013**, *4*, 4366−4374.

(54) Liang, Z.; Wu, X.; Yang, Y.-W.; Li, C.; Wu, G.; Gao, H. *Polym. Chem.* **2013**, *4*, 3514−3523.

(55) Lu, X.; Gao, H.; Li, C.; Yang, Y.-W.; Wang, Y.; Fan, Y.; Wu, G.; Ma, J. *Int. J. Pharm.* **2012**, *423*, 195−201.

(56) Wang, C.; Wang, Z.; Zhang, X. *Acc. Chem. Res.* **2012**, *45*, 608−618.

(57) Kim, B.-S.; Lee, H.-i.; Min, Y.; Poon, Z.; Hammond, P. T. *Chem. Commun.* **2009**, 4194−4196.

(58) Smith, R. C.; Riollano, M.; Leung, A.; Hammond, P. T. *Angew. Chem., Int. Ed.* **2009**, *48*, 8974−8977.

(59) Schmidt, D. J.; Moskowitz, J. S.; Hammond, P. T. *Chem. Mater.* **2010**, *22*, 6416−6425.

(60) de Villiers, M. M.; Otto, D. P.; Strydom, S. J.; Lvov, Y. M. *Adv. Drug Delivery Rev.* **2011**, *63*, 701−715.

(61) de Villiers, M. M.; Lvov, Y. M. *Adv. Drug Delivery Rev.* **2011**, *63*, 699−700.

(62) Ariga, K.; Lvov, Y. M.; Kawakami, K.; Ji, Q.; Hill, J. P. *Adv. Drug Delivery Rev.* **2011**, *63*, 762−771.

(63) Poon, Z.; Chang, D.; Zhao, X.; Hammond, P. T. *ACS Nano* **2011**, *5*, 4284−4292.

(64) Min, Y.; Hammond, P. T. *Chem. Mater.* **2011**, *23*, 5349−5357.

(65) DeMuth, P. C.; Moon, J. J.; Suh, H.; Hammond, P. T.; Irvine, D. J. *ACS Nano* **2012**, *6*, 8041−8051.

(66) Hammond, P. T. *Mater. Today* **2012**, *15*, 196−206.

(67) Wu, J.; Isaacs, L. *Chem.—Eur. J.* **2009**, *15*, 11675−11680.

(68) Lee, D.-W.; Park, K. M.; Banerjee, M.; Ha, S. H.; Lee, T.; Suh, K.; Paul, S.; Jung, H.; Kim, J.; Selvapalam, N.; et al. *Nat. Chem.* **2011**, *3*, 154−159.

(69) Dsouza, R. N.; Pischel, U.; Nau, W. M. *Chem. Rev.* **2011**, *111*, 7941−7980.

(70) Moghaddam, S.; Yang, C.; Rekharsky, M.; Ko, Y. H.; Kim, K.; Inoue, Y.; Gilson, M. K. *J. Am. Chem. Soc.* **2011**, *133*, 3570−3581.

(71) Lagona, J.; Mukhopadhyay, P.; Chakrabarti, S.; Isaacs, L. *Angew. Chem., Int. Ed.* **2005**, *44*, 4844−4870.

(72) Masson, E.; Ling, X.; Joseph, R.; Kyeremeh-Mensah, L.; Lu, X. *RSC Adv.* **2012**, *2*, 1213−1247.

(73) Tang, H.; Fuentealba, D.; Ko, Y. H.; Selvapalam, N.; Kim, K.; Bohne, C. *J. Am. Chem. Soc.* **2011**, *133*, 20623−20633.

6430

dx.doi.org/10.1021/cm503304p | *Chem. Mater.* 2014, 26, 6418−6431

(74) Lee, T. C.; Scherman, O. A. *Chem.—Eur. J.* **2012**, *18*, 1628−1633.

(75) Vinciguerra, B.; Cao, L.; Cannon, J. R.; Zavalij, P. Y.; Fenselau, C.; Isaacs, L. *J. Am. Chem. Soc.* **2012**, *134*, 13133−13140.

(76) Kim, C.; Agasti, S. S.; Zhu, Z.; Isaacs, L.; Rotello, V. M. *Nat. Chem.* **2010**, *2*, 962−966.

(77) Yang, H.; An, Q.; Zhu, W.; Li, W.; Jiang, Y.; Cui, J.; Zhang, X.; Li, G. *Chem. Commun.* **2012**, *48*, 10633−10635.

(78) Liu, S.; Ruspic, C.; Mukhopadhyay, P.; Chakrabarti, S.; Zavalij, P. Y.; Isaacs, L. *J. Am. Chem. Soc.* **2005**, *127*, 15959−15967.

(79) Hettiarachchi, G.; Nguyen, D.; Wu, J.; Lucas, D.; Ma, D.; Isaacs, L.; Briken, V. *PLoS One* **2010**, *5*, e10514.

(80) Propidium iodide is a plasma membrane-impermeable fluorescent dye and released from nanoparticles in the cells with pH stimulus, resulting in staining of the nuclei. See: Lu, J.; Choi, E.; Tamanoi, F.; Zink, J. I. *Small* **2008**, *4*, 421−426.

(81) These LbL materials enter inside the cells through endocytosis because MSN-based materials possess high affinities toward phospholipid. See: Mornet, S.; Lambert, O.; Duguet, E.; Brisson, A. *Nano Lett.* **2005**, *5*, 281−285. So, MSN can be adsorbed on the surface of cells to be endocytosed. In addition, clathrin-mediated endocytosis plays a key role in MSN delivery systems. See: Huang, D.-M.; Hung, Y.; Ko, B.-S.; Hsu, S.-C.; Chen, W.-H.; Chien, C.-L.; Tsai, C.-P.; Kuo, C.-T.; Kang, J.-C.; Yang, C.-S.; Mou, C.-Y.; Chen, Y.-C. *FASEB J.* **2005**, *19*, 2014−2016. Lin, Y.-S.; Tsai, C.-P.; Huang, H.-Y.; Kuo, C.-T.; Hung, Y.; Huang, D.-M.; Chen, Y.-C.; Mou, C.-Y. *Chem. Mater.* **2005**, *17*, 4570−4573 Meanwhile, MSN can escape from cytolysosome because of the clathrin protection..

(82) Ge, Z.; Liu, S. *Chem. Soc. Rev.* **2013**, *42*, 7289−7325.

(83) Gessner, A.; Waicz, R.; Lieske, A.; Paulkeb, B.-R.; Mädera, K.; Müllera, R. H. *Int. J. Pharm.* **2000**, *196*, 245−249.

(84) The phenomenon of the EPR effect is that cancer cells must stimulate the production of blood vessels to grow quickly. And vascular endothelial growth factor and other growth factors are concerned in cancer angiogenesis. Cancer cell aggregates as small as 150−200 μm start to become dependent on blood supply carried out by neovasculature for their nutritional and oxygen supply. These newly shaped tumor vessels are usually irregular in appearance and architecture. They are weakly associated defective endothelial cells with wide fenestrations, lacking a smooth muscle layer, or innervation with a wider lumen, and impaired serviceable receptors for angiotensin II. Additionally, tumor tissues usually lack effective lymphatic drainage. All these factors lead to irregular molecular and fluid transport dynamics, especially for macromolecular drugs. See: Ge, Z.; Liu, S. *Chem. Soc. Rev.* **2013**, *42*, 7289−7325. However, the consuming effect of macrophage depends on the surface feature of these dangerous materials. Macrophages can only swallow the materials that are more hydrophobic than them. Therefore, hydrophilic poly(ethylene glycol) (PEG) has been widely used to coat on the surface of a drug delivery system to reduce the phagocytosis of macrophage. Therefore, the mechanism of EPR effect is different from the PEG effect, and will not affect the macrophages clearance. See: Gessner, A.; Waicz, R.; Lieske, A.; Paulke, B.-R.; Mäder, K.; Müller, R. H. *Int. J. Pharm.* **2000**, *196*, 245−249. Zahr, A. S.; Davis, C. A.; Pishko, M. V. *Langmuir* **2006**, *22*, 8178−8185.

(85) Green, D. R.; Reed, J. C. *Science* **1998**, *281*, 1309−1312.

(86) Ac-DEVD-AFC is a fluorogenic substrate for CPP32 and related cysteine proteases, which has a Stokes shift superior to that of Ac-DEVD-AMC once it has been cleaved. CPP32 is involved in the cleavage of Ac-DEVD-AFC. See: Liu, L.; Peng, J.; Liu, K.; Yang, H.; Li, Y.; Hong, H. *Cell Biol. Int.* **2007**, *31*, 996−1001.

(87) Deng, Z. J.; Morton, S. W.; Ben-Akiva, E.; Dreaden, E. C.; Shopsowitz, K. E.; Hammond, P. T. *ACS Nano* **2013**, *7*, 9571−9584.

(88) Day, A.; Arnold, A. P.; Blanch, R. J.; Snushall, B. *J. Org. Chem.* **2001**, *66*, 8094−8100.